Strong Oxygen Participation in the Redox Governing the Structural and Electrochemical Properties of Na-Rich Layered Oxide Na2 IrO3

Arnaud J. Perez, Dmitry Batuk, Matthieu Saubanère, Gwenaelle Rousse, Dominique Foix, Eric Mccalla, Erik J. Berg, Romain Dugas, Karel H. W. van den Bos, Marie-Liesse Doublet, et al.

▶ **To cite this version:**

Arnaud J. Perez, Dmitry Batuk, Matthieu Saubanère, Gwenaelle Rousse, Dominique Foix, et al.. Strong Oxygen Participation in the Redox Governing the Structural and Electrochemical Properties of Na-Rich Layered Oxide Na2 IrO3 . Chemistry of Materials, 2016, 28 (22), pp.8278 - 8288. 10.1021/acs.chemmater.6b03338 . hal-01405732

HAL Id: hal-01405732

https://hal.sorbonne-universite.fr/hal-01405732

Submitted on 30 Nov 2016

HAL is a multi-disciplinary open access archive for the deposit and dissemination of scientific research documents, whether they are published or not. The documents may come from teaching and research institutions in France or abroad, or from public or private research centers.

L'archive ouverte pluridisciplinaire **HAL**, est destinée au dépôt et à la diffusion de documents scientifiques de niveau recherche, publiés ou non, émanant des établissements d'enseignement et de recherche français ou étrangers, des laboratoires publics ou privés.

Strong oxygen participation in the redox governing the structural and electrochemical properties of Na-rich layered oxide Na_2IrO_3

Arnaud J. Perez[1,2], Dmitry Batuk[1,3], Matthieu Saubanère[1,4,5], Gwenaelle Rousse[1,2,4], Dominique Foix[4,6], Eric McCalla[1,4,7], Erik J. Berg[8], Romain Dugas[1,4], Karel H.W. van den Bos[3], Marie-Liesse Doublet[4,5], Danielle Gonbeau[4,6], Artem M. Abakumov[3,9], Gustaaf Van Tendeloo[3] and Jean-Marie Tarascon[1,2,4*]

[1]Collège de France, Chimie du Solide et de l'Energie, UMR 8260, 11 place Marcelin Berthelot, 75231 Paris Cedex 05, France

[2]Sorbonne Universités - UPMC Univ Paris 06, 4 Place Jussieu, F-75005 Paris, France

[3]EMAT, University of Antwerp, Groenenborgerlaan 171, B-2020, Antwerp, Belgium

[4]Réseau sur le Stockage Electrochimique de l'Energie (RS2E), FR CNRS 3459, France

[5]Institut Charles Gerhardt, CNRS UMR 5253, Université Montpellier, Place E. Bataillon, 34 095 Montpellier, France

[6]IPREM/ECP (UMR 5254), University of Pau, 2 av. Pierre Angot, 64053 Pau Cedex 9, France

[7]CEMS, University of Minnesota, 421 Washington Ave., Minneapolis, MN, USA, 55455.

[8]Paul Scherrer Institut, Electrochemistry Laboratory, CH-5232 Villigen PSI, Switzerland

[9]Skoltech Center for Electrochemical Energy Storage, Skolkovo Institute of Science and Technology, 143026 Moscow, Russia

* Corresponding author: jean-marie.tarascon@college-de-france.fr

Abstract

The recent revival of the Na-ion battery concept has prompted intense activities in the search for new Na-based layered oxide positive electrodes. The largest capacity to date was obtained for a Na-deficient layered oxide that relies on cationic redox processes only. To go beyond this limit, we decided to chemically manipulate these Na-based layered compounds in a way to trigger the participation of the anionic network. We herein report the electrochemical properties of a Na-rich phase Na_2IrO_3, which can reversibly cycle 1.5 Na^+ per formula unit while not suffering from oxygen release nor cationic migrations. Such large capacities, as deduced by complementary XPS, X-ray/neutron diffraction and transmission electron microscopy measurements, arise from cumulative cationic and anionic redox processes occurring simultaneously at potentials as low as 3.0 V. The inability to remove more than 1.5 Na^+ is rooted in the formation of an O1-type phase having highly stabilized Na sites as confirmed by DFT calculations, which could rationalize as well the competing metal/oxygen redox processes in Na_2IrO_3. This work will help to define the most fertile directions in the search for novel high energy Na-rich materials based on more sustainable elements than Ir.

Introduction

The development of new and more efficient energy storage systems is a crucial technological challenge to facilitate the transition from fossil fuels to renewable energy sources. Since their first commercialization 25 years ago, Li-ion batteries have imposed themselves as the dominant technology for portable electronics and automotive applications. However, the relatively narrow distribution of Li resources on the planet has triggered renewed interest in alternative electrochemical storage systems. The Na-ion technology, which was first investigated along with Li-ion systems, is now the focus of abundant research. Its commercial success will largely rely on the development of cathode materials with both high energy density and long cyclability. Na-based layered oxides, with Na_xMO_2 formula (M = transition metal), provide a great versatility of compositions and structures, offering an opportunity to tune their electrochemical properties. However, most of these layered oxides present a limited energy density because of their low Na content together with their low redox voltage. The P2-$Na_{2/3}[Fe_{1/2}Mn_{1/2}]O_2$ phase, which contains ~0.7 Na per formula unit and shows a redox voltage of ~2.8 V vs Na^+/Na, has achieved the best performance (140 mAh/g) up to now[1]. To alleviate this energy density issue, research is presently parted between searching for i) new polyanionic compounds besides $Na_3V_2(PO_4)_2F_3$, which shows a higher redox voltage (~3.6 V vs Na^+/Na) for a capacity of 120 mAh/g and ii) new enriched layered Na-phases having larger capacities. We have taken the latter direction based on the learning from Li-rich layered oxides.

These Li-rich layered phases made of Ni, Co and Mn with Li in excess (e.g. $Li[Li_{0.2}Ni_{0.13}Mn_{0.54}Co_{0.13}]O_2$) have been shown to have capacities exceeding 270 mAh/g. Through complementary XPS, EPR, HRTEM and neutron diffraction experiments and using model compounds containing 4d/5d elements[2–5], such large capacities were shown to be nested, aside

from the classic cationic redox process, in the redox activity of the anionic network via the reversible formation of peroxo-like species. In light of such findings, new Li-rich layered materials exceeding 300 mAh/g ($Li_{1.2}Nb_{0.5}Mn_{0.5}O_2$)[6] or even reaching 350 mAh.g ($Li_4Mn_2O_5$)[7] have been discovered.

Similarly, in looking for Na phases with extra capacities, we decided to deviate from the single-minded cationic redox approach and manipulate Na-based compounds in a way to trigger the participation of the anionic network. The possibility of using Na-rich layered materials, with Na_2MO_3 formula, has been proposed by our group through the study of the solid-solution family $Na_2Ru_{1-y}Sn_yO_3$ (y = 0 to 0.75)[8], and further investigated by Yamada and coworkers for Na_2RuO_3.[9] Na-rich materials present reversible capacities exceeding 1 Na per formula unit, which is made possible by the high initial Na content together with the triggering of anionic redox activity.

However, as is often the case, materials showing new phenomena also come with some issues. The first one deals with progressive voltage decay upon cycling that was shown to originate from irreversible migration of cations to tetrahedral sites during cycling. A second problem observed in Li-rich materials is related to their capacity losses upon cycling, which are often associated to O_2 gas release. Indeed, the O_2^{n-} species, depending upon their forming potential (above ~ 4.3 V vs. $Li^+/Li°$), can be unstable against oxygen recombination and lead to O_2 release. To minimize this issue, one needs to increase the M-O covalency with the proper substitution as was done in moving from 3d (Mn) to 4d (Ru) or 5d (Ir) metals. In the latter case, the high covalence prevents cationic migrations and Li_2IrO_3 moves from an O3 to an O1 structure in order to alleviate the stress associated with Li removal, hence enabling the visualization of (O-O) dimers[10]. This work was very recently extended with a similar behavior in $LiRhO_2$, where

$(O_2)^{n-}$ peroxo-like species with O-O distances as short as 2.26 Å were also observed at high voltage and their strong covalent bonding to Rh was claimed to prevent O_2 release.[11]

When switching to Na-ion compounds, open questions remain. How the insertion/deinsertion of large and highly polarizable *guest* ions (Na^+) into these *host* rocksalt oxide structures affects the anionic redox mechanism, the ligand hole chemistry, the massive cation migration and capture in interstitial tetrahedral sites, and the stability of the reactive $(O_2)^{n-}$ oxygenated species towards the release of O_2 during electrode charging ? To address these seminal questions, we decided, for the sake of simplicity, to study the Na-based iridium phase Na_2IrO_3 with the hope to bypass O_2 release and cation migration. Herein we show that Na_2IrO_3 can reversibly release and uptake 1.5 Na^+ per formula unit, through well-defined structural changes. We demonstrate that these changes are driven by the increased cationic repulsion in the material associated with charge density loss on O atoms. If the anionic redox process was found to be reversible, the long-term cycling performances of this material were found to be very sensitive to the degradation of the electrolyte.

Experimental

Synthesis: Na_2IrO_3 was synthesized using the method reported by Krizan et al.[12] Metallic Ir (Alfa Aesar, 325 mesh, 99.9%) and Na_2CO_3 (Sigma Aldrich, 99.5%) with 10 % excess were mixed using a mortar and pestle and heated in air at 800°C for 48h in a covered alumina crucible. The furnace was slowly cooled (1°C/min) to 600°C and the sample was quickly transferred to an argon-filled glovebox to avoid reaction with moisture or carbon dioxide from the air upon cooling. A small amount of IrO_2 was still present after the first step due to an incomplete reaction of the precursors, therefore the sample was ground again and heated a second time in air at 900°C for 24h, cooled slowly (1°C/min) to 600°C and transferred once more to the glovebox.

Electrochemistry: Electrochemical characterization was performed in Swagelok-type cells for *ex situ* studies and 2.032-type coin cells for long-term cycling properties. The positive electrode consisted of Na_2IrO_3 ball-milled for 20 minutes with 20 wt% carbon SP using a SPEX 8000m Mill, and metallic Na was used as an anode. Positive and negative electrodes were separated by a Whatman GF/D borosilicate glass fiber membrane soaked with 1M $NaClO_4$ or $NaPF_6$ in ethylene carbonate (EC) : dimethyl carbonate (DMC) (1 : 1 weight ratio), with or without 1 wt% fluorinated ethylene carbonate (FEC) as an additive. All parts were assembled in an Ar-filled glovebox. Galvanostatic cycling was performed at a C/5 rate (1 Na^+ removed in 5h) between 1.5 and 4 V versus Na^+/Na. After cycling, samples for *ex situ* characterization were recovered inside the glovebox and washed three times in anhydrous DMC. Cycling in full cells configurations was done using hard carbon as an anode, and 1M $NaPF_6$ in EC : DMC as an electrolyte.

X-ray and Neutron Powder Diffraction experiments: X-ray powder diffraction (XRD) patterns of pristine and *ex situ* samples were measured using a BRUKER D8 Advance diffractometer with

Cu Kα radiation ($\lambda_{K\alpha1}$=1.54056 Å, $\lambda_{K\alpha2}$=1.54439 Å). To limit exposure to air for sensitive samples, airtight sample holders equipped with a Kapton window were used. *In situ* XRD was done using an electrochemical cell equipped with a Be window. Na_2IrO_3 was charged to 4.3 V and discharged to 1.5 V at C/20, while measuring 1h XRD scans in the 2θ range 12-60°. Synchrotron X-ray diffraction (SXRD) was performed on the 11-BM beamline (Advanced Photon Source, Argonne National Laboratory) with a wavelength of 0.414206 Å, using sealed quartz capillaries to prevent air exposure. Neutron Diffraction (ND) patterns were measured for the pristine material on the D20 powder diffractometer (Institut Laue-Langevin) in its high-resolution mode (take-off angle 90°), with a wavelength λ = 1.5444 Å. *Ex situ* samples were measured on HRPT high-resolution neutron powder diffractometer (Swiss Spallation Neutron Source SINQ, Paul Scherrer Institute) with a wavelength of 1.494 Å. Samples were loaded in sealed Ø=5mm vanadium cylindrical cans in an argon-filled glovebox. Rietveld refinements were made using the FullProf suite[13] and the program FAULTS[14] was used to account for stacking faults in the structure. The strong absorption of neutron by Ir was taken into account for the refinements.

X-ray photoemission spectroscopy: X-ray photoemission spectroscopy (XPS) measurements were carried out with a Kratos Axis Ultra spectrometer, using focused monochromatic Al Kα radiation (hν = 1486.6 eV). The XPS spectrometer was directly connected through a transfer chamber to an argon dry box, in order to avoid moisture/air exposure of the samples. The analyzed area of the samples was 300 × 700 μm^2. Peaks were recorded with constant pass energy of 20 eV. For the Ag $3d_{5/2}$ line the full width at half-maximum (FWHM) was 0.58 eV under the recording conditions. The pressure in the analysis chamber was around 5×10^{-9} mbar. Short acquisition time spectra were recorded before and after each normal experiment to check that the

samples did not suffer from degradation during the measurements. The binding energy scale was calibrated using the C 1s peak at 285.0 eV from the hydrocarbon contamination invariably present. To avoid any error on the calibration choice and for more precision, the binding energy difference between the O1s lattice and metal core peaks was also determined. Core peaks were analyzed using a nonlinear Shirley-type background[15]. The peak positions and areas were optimized by a weighted least-square fitting method using 70% Gaussian, 30% Lorentzian line shapes. Quantification was performed on the basis of Scofield's relative sensitivity factors[16]. The curves fit for core peaks were obtained while minimizing the number of peaks used to fit the experimental curves.

Electron microscopy: Samples for the transmission electron microscopy (TEM) investigation were prepared by grinding powdered samples in a mortar and dipping holey carbon TEM grids into the powder. To prevent exposure of the samples to air they were stored and prepared for TEM in an Ar filled glovebox. A special Gatan vacuum transfer holder was used for the analyses. Electron diffraction (ED) data, high-resolution high angle annular dark field scanning transmission electron microscopy (HAADF-STEM) and annular bright field STEM (ABF-STEM) images were acquired on a probe aberration corrected FEI Titan 80-300 electron microscope at 300 kV. Cation composition of the samples at different charge/discharge states was confirmed using energy dispersive X-ray (EDX) analysis. The data were collected on an FEI Osiris transmission electron microscope equipped with a Super-X EDX detector and operated at 200 kV.

Online Electrochemical Mass Spectrometry (OEMS): Electrodes of a final composition of 75:15:10 active material:conductive carbon:binder were prepared by first mixing partially charged $NaIrO_3$ and carbon SP powder with Kynar Flex binder (Solvay, Belgium) suspended in

N-methyl-2-pyrrolidinone (NMP; Sigma-Aldrich, Germany) to form a viscous slurry, which in turn was doctor-blade coated (150 μm) on a porous glass fiber sheet (Grade GF/C, Whatman®, UK) and dried under dynamic vacuum at 80°C overnight. Electrodes were punched (Ø 18 mm, ~9 mg active material loading) and again dried (120°C, dynamic vacuum), before being immediately brought into an Ar filled glovebox (< 5 ppm H_2O / O_2, MBraun, Germany). The OEMS cell was assembled with the electrode on top of a glass fiber separator (Ø 24 mm, Grade GF/C, Whatman®, UK) and a metallic Na disc (Ø 22 mm, ~0.5 mm thickness, Sigma-Aldrich, Germany); all of which was soaked in 150 μL electrolyte (1M $NaClO_4$ in 1:1 EC:DMC).

During operation, the magnetic valves were automatically opened/closed in order to probe the partial pressures of O_2 and CO_2 of the OEMS cell. For each measurement point, 0.7 mL of gas is extracted from the headspace (3.2 mL) of the cell for partial pressure analysis and replaced by pure Ar (Quality 5.0). Calibration gas bottles were utilized to relate the MS ion-current signal for O_2 (m/z=32) and CO_2 (m/z=44) to known gas concentrations of 2000 ppm O_2 in Ar and 500 ppm CO_2 in Ar, respectively, before and after the measurement. The cells were kept at OCV for 4h in order to flush any residual gases accumulated during cell assembly or mounting, before cycling in galvanostatic mode (~C/10) in a potential window of 1.5-4.2 V vs. Na^+/Na for two cycles, whereby the gas evolution was probed in 15 min intervals.

First-principles DFT calculations: Spin-polarized density functional theory (DFT) calculations were performed using the plane-wave density functional theory VASP (Vienna Ab initio Simulation Package) code[17,18] within the generalized gradient approximation of Perdew–Burke–Ernzerhof (PBE) to describe electron exchange and correlation.[19] The rotationally invariant Dudarev method[20] (DFT+U) was used to correct the self-interaction error of conventional DFT for correlated d-electrons. Crystal structures, electrochemical potentials and magnetic properties

of the Na_xIrO_3 phase were shown to be well reproduced at $U_{eff} = U - J = 2$ eV for Ir (J = 1 eV). The D3 dispersion correction of Grimme (DFT-D3)[21] was also applied to better describe the weak van der Waals interactions expected in these layered phases at low Na-contents. Spin-orbit coupling was also considered for the heavy iridium metal but did not significantly affect the results presented in the present paper. Conjugate gradient energy-minimization procedure were used to relax all atom coordinates and lattice parameters until the forces acting on each atom were less than 5.10^{-3} eV/A. A plane-wave cutoff of 600 eV was used to describe the atomic basis set, with well-converged k-point sampling for each compound. The COOPs were computed using the Lobster program developed by Dronskowski and coworkers.[22–24]

Results

Structure of pristine Na_2IrO_3

The structure of the as-prepared Na_2IrO_3, which can also be written as $Na[Na_{1/3}Ir_{2/3}]O_2$, is derived from the rocksalt structure, with a framework of cubic close-packed oxygens and cations occupying the octahedral sites. Segregation of Na^+ and Ir^{4+} cations leads to a layered structure, with pure Na layers alternating with mixed $NaIr_2$ layers, in which Ir^{4+} and Na^+ are distributed in a honeycomb pattern. Using the notation introduced by Delmas et al.[25], Na_2IrO_3 has an O3 structure, where O stands for the octahedral coordination of Na in the Na layers, and 3 for the number of $[Na_{1/3}Ir_{2/3}]O_2$ layers needed to describe the oxygen stacking (ABCABC).

The synchrotron X-ray powder diffraction pattern (Figure S1a) was refined using the Rietveld method and fitted with a monoclinic *C*2/*m* unit cell (a = 5.43004(3) Å, b = 9.40163(5) Å, c = 5.61095(2) Å and β = 108.9660(4)°). In order to obtain a good fit, it was necessary to introduce some site mixing between Ir and Na in the $NaIr_2$ layers. However, this is an artificial way to reduce the intensity of the superstructure peaks in the 5-8° 2θ region (λ = 0.414206 Å), and does not represent the real structure of the material. The asymmetric broadening of these superstructure peaks arises from the presence of stacking faults. TEM data for the pristine Na_2IrO_3 confirms the long-range ordered sequence of close-packed oxygen layers, corresponding to the O3-type structure (see [010] HAADF-STEM image in Figure 1c and the corresponding ED pattern in Figure S2a). The [100] HAADF-STEM image of this sample indicates perfect honeycomb cation ordering in the $NaIr_2$ layers, which can be seen by the rows of double closely projected Ir columns. However, numerous stacking faults are present, violating the perfect arrangement of the honeycomb layers (see Figure 1c and Figure S2b). Refinement of the

broadened superstructure peaks from the SXRD pattern can be done using the FAULTS software[14], by adjusting the relative probabilities of different possible stacking vectors (Figure S3). The shape of the superstructure peaks is best represented with a model using a combination of 30% of random stacking sequences and 70% of alternating short-range ordered stacking sequences. The X-ray diffraction pattern is dominated by the Ir contribution because of its high electron density, therefore complementary neutron powder diffraction was used to obtain the accurate O and Na positions. The final Rietveld refinement is shown in Figure S1b and Table S1 gathers the deduced structural information.

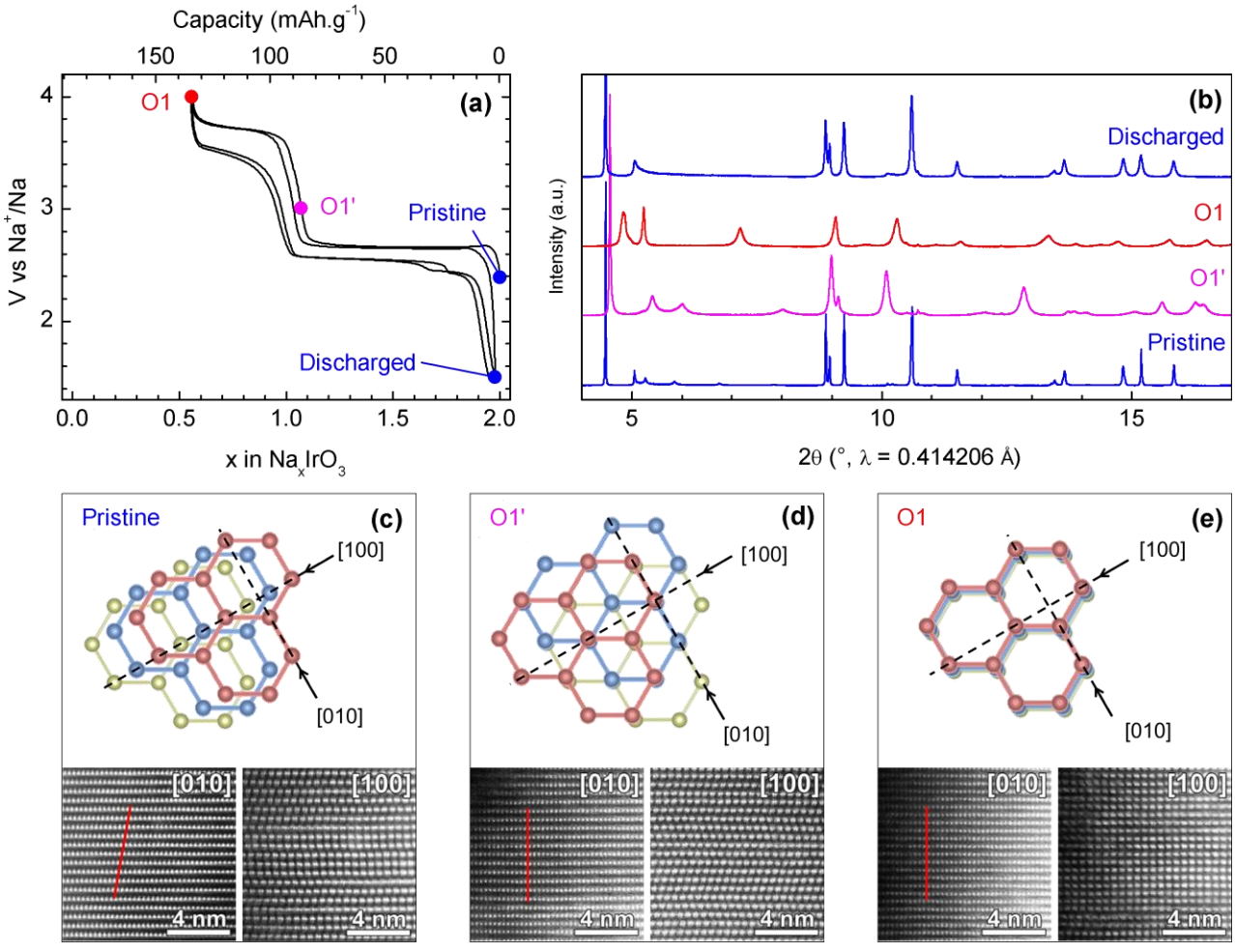

Figure 1

Electrochemical properties

Na_2IrO_3 was cycled in a Na half-cell between 1.5 V and 4 V at a C/5 rate (1 Na removed in 5 h). At first, NaPF6 or $NaClO_4$ (1 M) in ethylene carbonate (EC)/dimethyl carbonate (DMC) (1:1) were used as electrolytes, but a strong irreversible capacity and a rapid capacity decay were observed. Therefore, 1% of fluoroethylene carbonate (FEC) was used as an additive in $NaClO_4$:EC:DMC since it enables high coulombic efficiency in Na half-cells, as reported by several groups.[26,27] The first two charge-discharge cycles are shown in Figure 1a. During the first charge, the Na^+ deintercalation proceeds through two plateaus at 2.7 V ($2.0 > x > 1.0$) and 3.7 V ($1.0 > x > 0.5$), respectively. They correspond to a cumulative removal of 1.5 Na^+, which are fully reinserted on the subsequent discharge, leading to a reversible capacity of 130 $mAh.g^{-1}$.

Unlike most Li-rich materials, the two plateaus are well preserved through the discharge on subsequent cycles. Such a behavior might indicate that, alike to Li_2IrO_3, the Na_2IrO_3 material does not demonstrate pronounced Ir migration upon cycling, which is further confirmed by our TEM data (Figure 1e and S4). To check for the possible release of oxygen upon cycling, an Online Electrochemical Mass Spectrometry experiment was performed. It resulted in a very small O_2 release on the first and second cycles (Figure 2) at the very end of charge (> 3.8 V). This small quantity would correspond to only 0.06 % of the total oxygen content in the material if it was solely attributed to oxygen release from Na_2IrO_3. Lastly, the release of CO_2 is worth mentioning. We believe that its origin is rooted in the decomposition of the carbonates at the surface of Na, while we cannot fully eliminate the possibility of having some CO_2 coming from the reaction of the electrolyte with surface oxygens. This is quite unlikely, bearing in mind the good reversibility of half-cells containing FEC, implying that the oxygen content in Na_2IrO_3 is not affected through the first cycle.

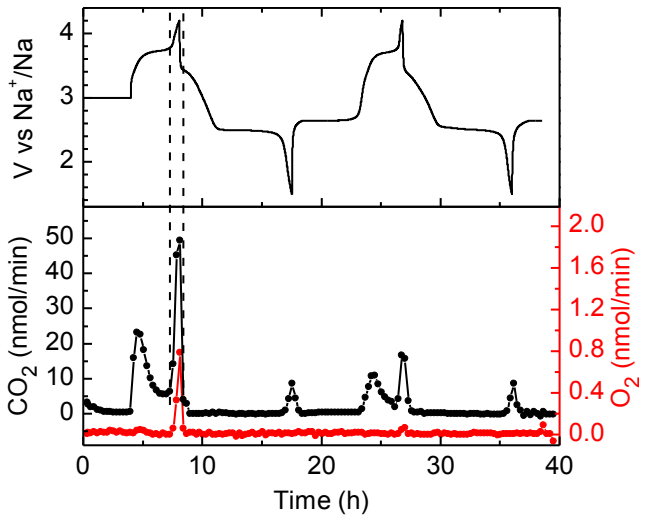

Figure 2

Structural changes on charge and discharge

In situ XRD was used to probe the structural evolution of Na_2IrO_3 during the first cycle (Figure 3). The first plateau appears to be composed of two distinct processes: first a solid solution with a modification of the lattice cell parameters, followed by a two-phase process, with the pristine phase disappearing at the expense of a new phase. The latter becomes pure at the end of the first plateau and has a composition close to $NaIrO_3$. The second plateau also corresponds to a two-phase process, leading to another phase with low Na content, close to $Na_{0.5}IrO_3$ (Na/Ir = 0.50(8) according to the EDX analysis). These new intermediate and final phases were further characterized by TEM, synchrotron XRD and ND.

Charging of the material to 3 V changes the staking of the oxygen sublattice from the cubic close-packed ABCABC arrangement, characteristic of the O3 structure, to the hexagonal close-packed ABAB arrangement (Figure 1d and Figure S2c,d). In this structure, hereafter referred to as O1', the Ir/Na sites are aligned on top of each other, with the honeycomb layers being systematically shifted with respect to the previous one. However, high concentration of stacking faults remains

in the stacking sequence of the honeycomb layers, which is evident from the HAADF-STEM image in Figure 1d and the corresponding electron diffraction pattern in Figure S2d. This intermediate phase with an approximate composition $NaIrO_3$ is similar to that obtained by Wallace and McQueen using a chemical oxidation method.[28] X-ray and neutron diffraction data for this structure can be indexed using a $P\bar{1}$ space group with the cell parameters a = 5.28226(14) Å, b = 5.27079(14) Å, c = 5.99680(17) Å, α = 115.564(2)°, β = 90.121(3)° and γ = 119.761(2)° (Figure S5 and Table S2).

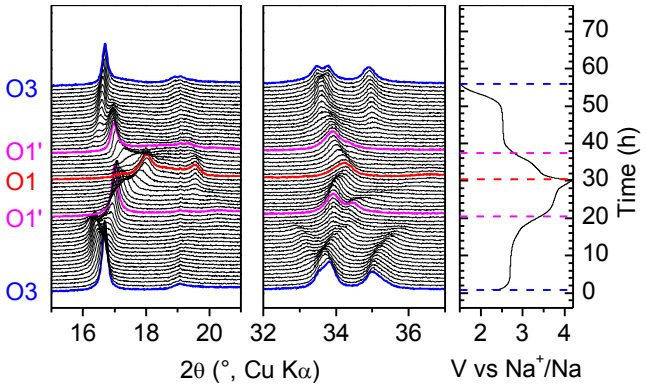

Figure 3

Further charge up to 4 V (chemical composition $Na_{0.5}IrO_3$) results in a reorganization of the metallic layers but with the same ABAB oxygen stacking sequence. The O1 structure obtained differs from the previous O1' by a complete suppression of the lateral shifts of the honeycomb layers (Figure 1e and S2e,f), so that the transition metal layers are stacked exactly on top of each other. This structure is similar to that obtained on full charge for Li_2IrO_3. The corresponding X-ray and neutron diffraction profiles can be indexed using a $C2/m$ space group with cell parameters a = 5.2534(2) Å, b = 9.0633(2) Å, c = 4.88271(19) Å and β = 89.482(17)° (Figure 4, 6b and Table S3). However, complete and satisfying Rietveld refinements of the O1 and O1' diffraction patterns are hindered because of the presence of very broad and asymmetric peaks,

probably related to anisotropic strain and stacking faults in the crystals. This can nicely be viewed in the inset of Figure 4, which highlights the peculiar and asymmetric broadening of the (001) peak, pointing to a non-uniform distribution of interlayer distances in the O1 structure. Upon first discharge to 1.5 V, the material transforms back to the O3 structure with well-ordered stacking of the O layers, but nearly random stacking of the honeycomb layers (Figure S4a,b and S7, Table S4), which results in a pronounced broadening of superstructure peaks (Figure S3).

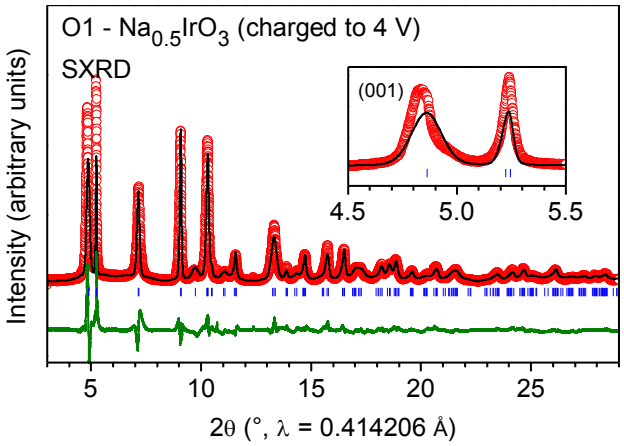

Figure 4

Cationic and anionic participations in the redox activity

Similar to the Li-rich materials, the 130 mAh·g^{-1} reversible capacity on the first cycle cannot be explained only by a classical cationic redox mechanism. X-ray photoemission spectroscopy (XPS) was used to probe the electronic changes of iridium and oxygen upon the first charge process. Figure 5 shows the evolution of Ir 4f and O 1s peaks for Na_xIrO_3 with x = 2.0 (pristine), 1.5 (pristine + O1'), 1.0 (O1') and 0.5 (O1). The Ir 4f peaks shifts towards higher binding energy during the first plateau (2.0 > x > 1.0), indicative of the oxidation of Ir^{4+}, and broadens for x = 1.5 as this corresponds to a biphasic composition of O3-Na_2IrO_3 and O1'-$NaIrO_3$. At x = 1.0, the shape of the Ir 4f peak recovers its original width. The Ir peak does not shift upon further removal

of Na ($1.0 > x > 0.5$), suggesting that iridium is not involved in the redox mechanism at high potential. Turning to the corresponding evolution of the O 1s peaks, we observe the emergence of a peak indicating oxidized oxygen species $(O_2)^{n-}$ as soon as 0.5 Na^+ is removed and its relative intensity keeps increasing until full charge. We can thus conclude that both iridium and oxygen redox processes are responsible for the electrochemical activity of the material on the first plateau ($2.0 > x > 1.0$), whereas the second plateau ($1.0 > x > 0.5$) seems to be only due to oxygen redox. The coexistence of both cationic and anionic activity on the low voltage plateau was previously shown for Li_2IrO_3, which was also subject to a structural transition from O3 to O1 upon delithiation.[10]

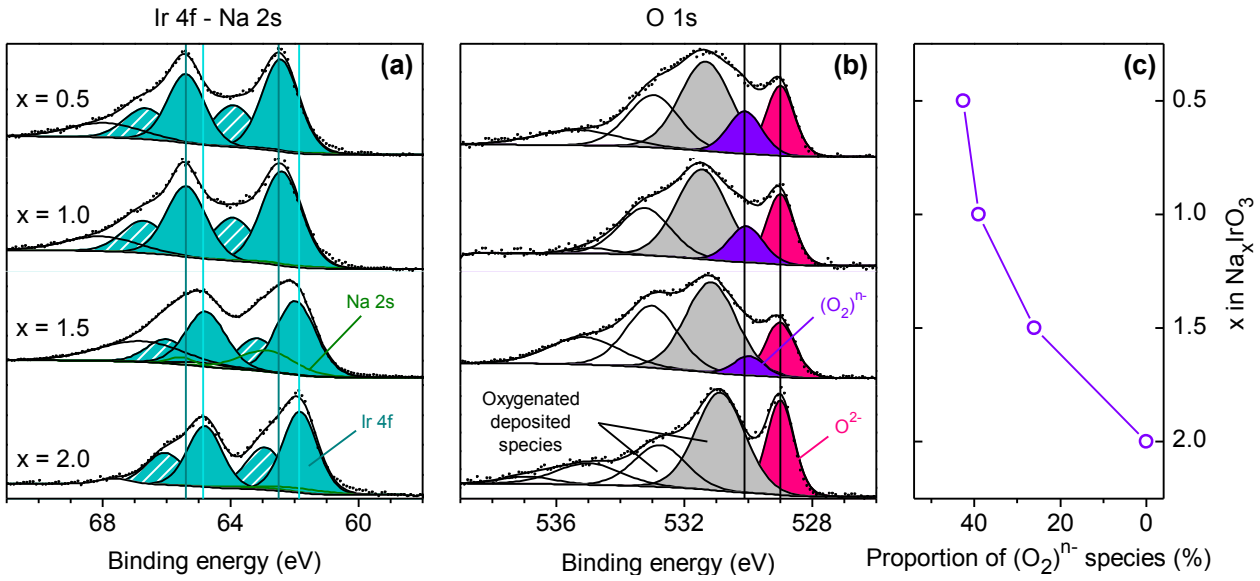

Figure 5

The specific ordering of the fully charged O1 structure, with the honeycomb layers aligned on top of each other, provides a clear projection of both the oxygen and cation sublattices along the [001] axis (Figure 6c-e), where the cation and oxygen columns can be viewed separately. We used this opportunity to visualize O atomic columns using the ABF-STEM imaging technique as

reported recently for the $Li_{0.5}IrO_3$ structure.[10] In the [001] ABF-STEM image (Figure 6d), the Ir columns appear as the darkest dots forming a hexagonal honeycomb pattern. Each Ir column is surrounded by 6 faint dots corresponding to the IrO_6 octahedra projected along their 3-fold symmetry axis. The dots centering the Ir hexagons can be attributed to the residual Na atoms. Absence of Ir and ordered location of Na in the hexagonal tunnels is evident from the comparison of [100] HAADF-STEM and ABF-STEM images (Figure S8): the Na atomic columns are visible in the ABF-STEM image and do not show up in the HAADF-STEM image due to relatively low atomic number of Na.

ABF intensity profiles (Figure 6f) clearly demonstrate two different sets of the projected O-O separations, with a formation of three longer and three shorter distances. Using the statistical parameter estimation method,[29] we analyzed the positions of the projected atomic columns in the image and measured that the average projected O-O distances are 2.07(4) Å and 1.33(3) Å for longer and shorter separations, respectively (Figure S9).

To confirm the presence of short and long O-O distances in the O1 structure, we compared the different O-O distances obtained from refinement of neutron diffraction data in the O3 and O1 structures (Figure 6a-b). In the pristine O3 material, short and long O-O distances already exist to a lesser extent, with the shortest bonds (2.668 Å) having a relative deviation of -8.3 % from the average O-O distance in the structure (2.909 Å). For the O1 oxidized sample, the average O-O distance is decreased to 2.837 Å as a result of Ir oxidation, and the shortest O-O bond is found to be 2.456 Å, which represents an increased deviation from the average distance of -13.4 %. Therefore, neutron diffraction fully confirms the TEM observations.

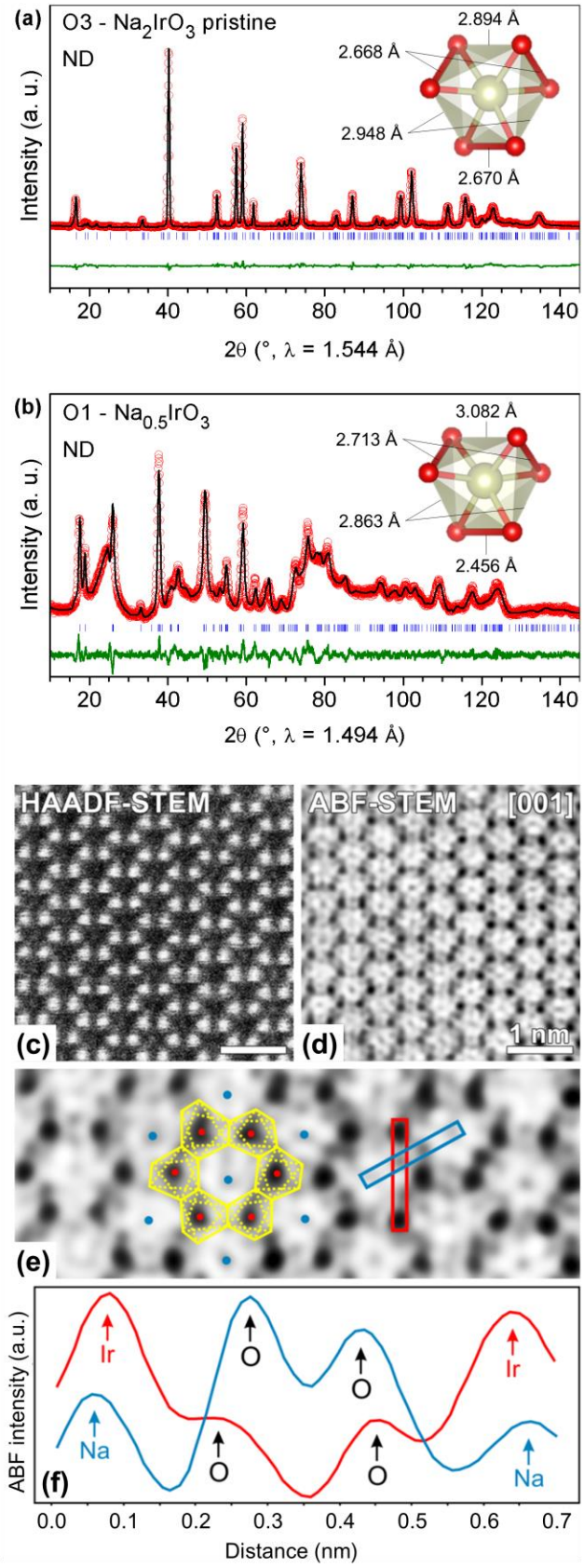
(a)
O3 - Na2IrO3 pristine
ND
Intensity (a. u.)
2.894 Å
2.668 Å
2.948 Å
2.670 Å
20 40 60 80 100 120 140
2θ (°, λ = 1.544 Å)
(b)
O1 - Na0.5IrO3
ND
Intensity (a. u.)
3.082 Å
2.713 Å
2.863 Å
2.456 Å
20 40 60 80 100 120 140
2θ (°, λ = 1.494 Å)
HAADF-STEM
ABF-STEM [001]
(c)
(d)
1 nm
(e)
ABF intensity (a.u.)
Ir
O
O
Ir
Na
O
O
Na
(f)
0.0 0.1 0.2 0.3 0.4 0.5 0.6 0.7
Distance (nm)

Figure 6

Capacity decay upon cycling

Figure 7a shows the long-term cycling performances of Na_2IrO_3. When cycling on the full voltage range (1.5 V to 4 V), the discharge capacity steadily decreases (Figure 7c), indicating a slow degradation process. To verify whether this decay arises from a low or high voltage process, the cycling was repeated on the lower plateau only with an upper cutoff of 3 V (Figure 7b). The reversibility of the low plateau is found to be good, indicating that the process hindering the reversibility of Na_2IrO_3 is a high voltage process. On the other hand, cycling on the high voltage plateau, between 2.6 and 4 V, was found to be poor with a rapid capacity decay and a gradual polarization on discharge.

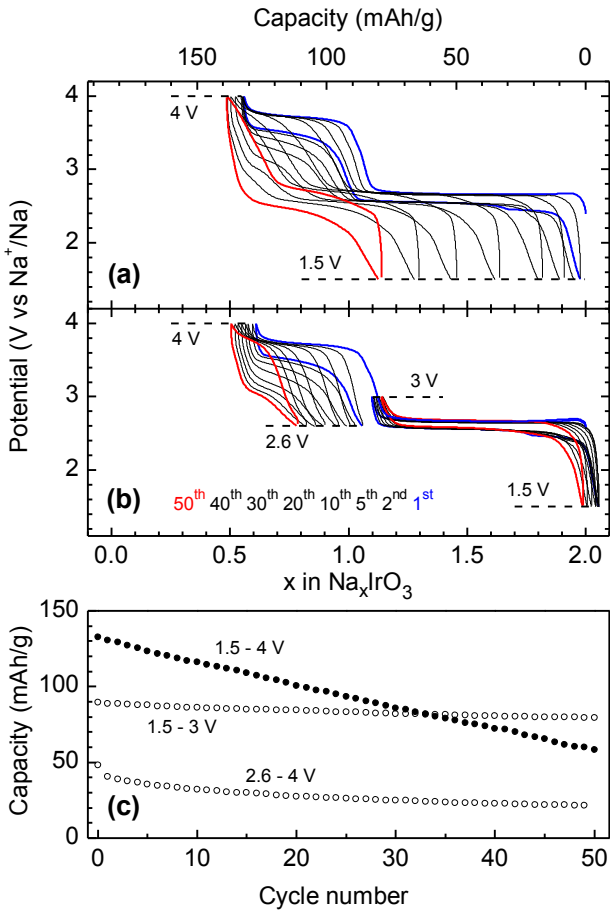

Figure 7

XRD analysis of the sample discharged after 50 cycles between 1.5 V and 4 V indicates the presence of both O3 phase and a new phase as shown in Figure 8. This new phase is very similar to the fully charged O1 phase, i.e. with hexagonal close packing of the O atoms and the honeycomb layers stacked perfectly on top of each other (see TEM data in Figure 8c,d). However, the unit cell parameters were very different, with a = 5.42839(11) Å and b = 9.3664(2) Å, close to those of the pristine structure, and c = 4.56187(7) Å, approximately 0.3 Å smaller than in the O1 structure (Figure 8a and Table S5). This new phase will be referred to as O1* and corresponds to a collapsed O1 phase, with a smaller interlayer distance. This result indicates that part of the sample undergoes an irreversible transition from O1 to O1* and remains blocked in the O1* structure, while the intact part of the material reversibly reinserts Na^+ through

the O1-O1'-O3 structural transitions. This gradual transformation of O1 to O1* results in a steady capacity decrease, as shown in Figure 7c. On the other hand, a low cutoff voltage at 3 V limits the structural transition to O3-O1' and the cycling is not hindered by the formation of the blocked O1* phase.

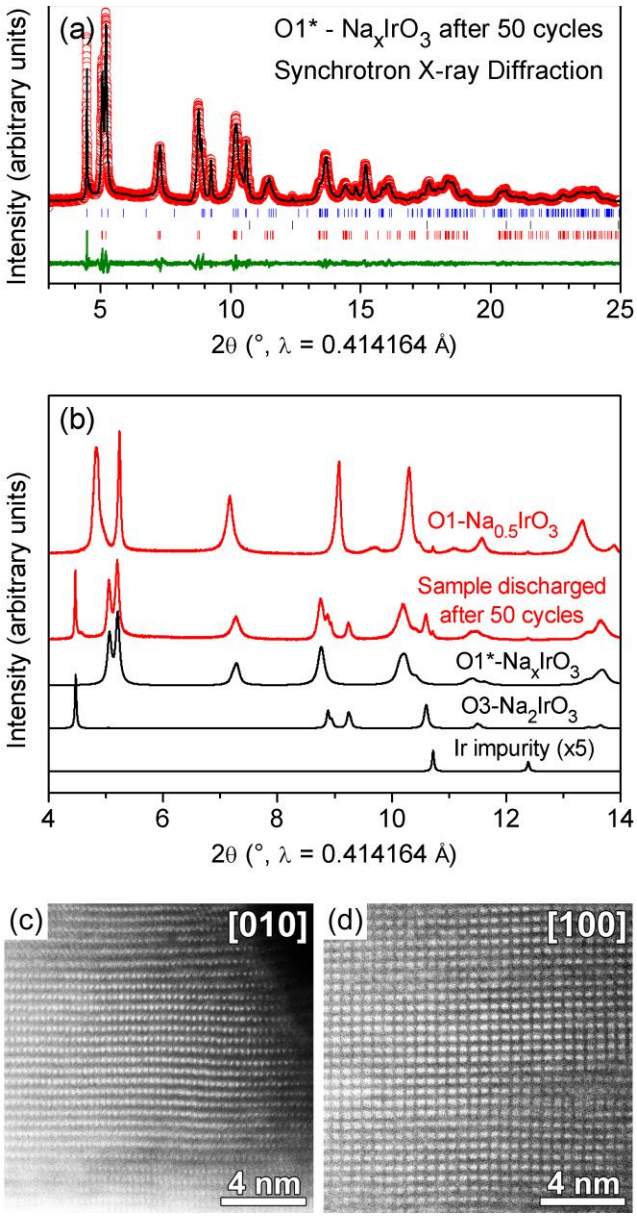

Figure 8

As mentioned previously, cycling without FEC led to a poor coulombic efficiency accompanied by fast capacity decay. The predominance of the O1* phase after most of the capacity was lost suggests a possible relation between electrolyte decomposition in the cell and degradation of the material. In order to avoid any electrolyte decomposition in contact with Na, Na_2IrO_3 was cycled in a full cell versus hard carbon and $NaPF_6$ in EC:DMC as an electrolyte (Figure 9a). Interestingly, the cell could cycle more than 150 cycles with barely any capacity decay. This full Na-ion cell delivers a reversible capacity of 96 $mAh.g^{-1}$, with a coulombic efficiency of 75.3 % on the first cycle, due to the formation of a SEI on the hard carbon anode, and more than 99.5 % on the next 150 cycles (Figure 9b). Such results further stress that the choice of electrolyte is critical for achieving long-term performance. Moreover, they highlight the full reversibility of the cumulative cationic and anionic process if we select the proper electrolyte formulation.

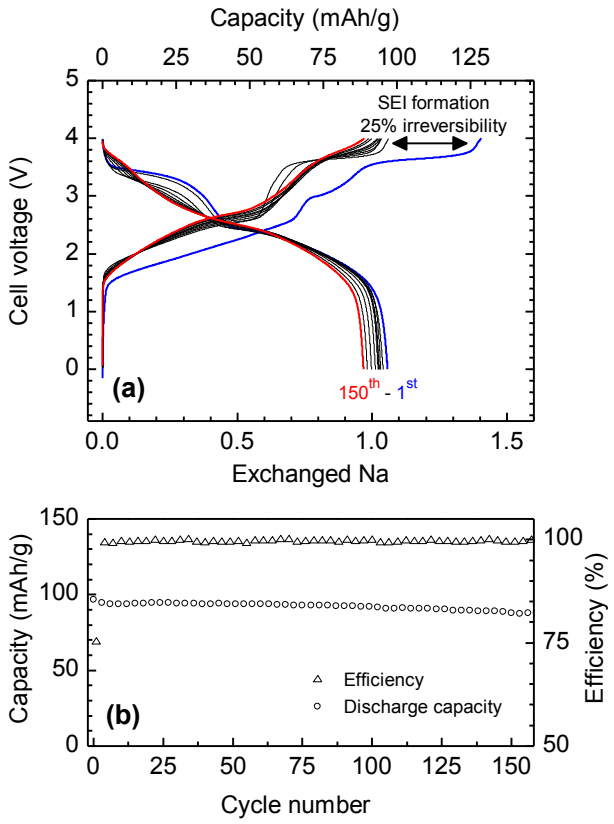

Figure 9

Theory

In the following, we offer a tentative rationalization of these structural/electrochemical results via first-principles DFT calculations. The crystal structures of the pristine, partially desodiated and fully desodiated materials obtained from full structural relaxations (Table S6) are in very good agreement with experiments. As expected, dispersion corrections need to be included at low Na-contents to account for weak van der Waals interlayer interactions, while at high Na-contents the interlayer spacing is dictated by electrostatics and is well reproduced by conventional DFT. Figure S10 shows that, among the different possible structural models for each Na content, the experimentally observed O3, O1' and O1 structures correspond to those presenting the lowest energies. At this stage, it is worth mentioning that the O1* collapsed structure experimentally observed after long cycling could not be found from structural relaxations, irrespective of the initial structure and the parameter settings (DFT, DFT-D3, U_{eff} value) considered in the calculations. Nevertheless, a 4.5 Å interlayer spacing matching well that of the O1* collapsed structure was found for the fully desodiated IrO_3 phase suggesting either that the Na-content deduced from the galvanostatic curves is slightly over-estimated or more likely that kinetic limitations lead to inhomogeneous Na-distributions in the particles.

Turning to the observed voltages, they can be nicely matched with the calculations if dispersion corrections are included. By adding the dispersions, the voltage increases from 2.20 V (DFT) to 2.74 V (DFT-D3) for the first plateau at 2.7 V associated to the O3 to O1' transformation and from 3.20 V to 3.58 V for the second plateau at 3.7 V corresponding to the O1' to O1 transformation. Note that if no transformations were occurring during these two successive oxidations, the associated calculated voltages would be significantly increased up to

3.0 V and 4.2 V, respectively. This is explained by the sodium Madelung potentials which are much lower in the partially desodiated O3-$NaIrO_3$ and O3-$Na_{0.5}IrO_3$ phases than in the O1'-$NaIrO_3$ and O1-$Na_{0.5}IrO_3$, in full agreement with the structural analysis conducted on the three polymorphs in Figure 10.

Discussion

The experimental data obtained from Na_2IrO_3 provide us with an opportunity to address several issues concerning i) the consequences of strong anionic participation to the overall redox process for highly desodiated structures, ii) the nature of material-electrolyte interaction and iii) the effect of the structure on the electrochemical performances in Na-rich layered oxides.

Previous studies have shown that Li-rich or Na-rich materials based on either 3d or 4d transition metals undergo through the first cycle a drastic evolution of their voltage profile, which evolves from a cascade (oxidation) to an S-shaped profile on reduction. Such a modification is linked to the Li-driven cationic migrations, which lead to irreversible local structural changes. This is no longer true with compounds based on 5d metals (e.g. Ir). The large delocalization of 5d orbitals enables a greater overlap with O 2p orbitals as compared to 3d or 4d metals. This results in strong covalent Ir-O bonds that block Ir migration from the metallic layers to the interlayer sites, as it was previously observed for Li_2IrO_3 and herein with Na_2IrO_3. [10] Another consequence of this strong overlap, is the early participation of oxygen to the redox properties as reported for Li_2IrO_3, and confirmed on Na_2IrO_3 by complementary XPS and high-resolution STEM data that reveal the presence of (O-O) dimers when only 0.5 Na^+ is electrochemically removed from Na_2IrO_3. This is unusual when compared to Ru-based materials, for which oxidation of Ru^{4+} and activation of the anionic process are totally decoupled and occur at low and high potential, respectively. This is also different from Li-rich NMC, which show a stair case profile, with the first plateau associated to the oxidation of antibonding Ni-O and Co-O orbitals, and the second one to the anionic process together with the release of oxygen at high voltage. Formation of O-O dimers has several important implications on the structural stability of the material. The shorter Ir-O bonds, together with the distortion of the oxygen lattice to form O-O dimers, lead to a contraction of the $NaIr_2O_6$

layers along the c direction. Oxygen charges are localized closer to the Ir planes, resulting in a lower screening of cationic repulsions between Na^+ in the Na planes and all other cations. This creates elastic stress in a direction parallel to the layers, which eventually promotes systematic shifts of the layers to minimize this stress. The O1' structure obtained after removing one Na^+ (Figure 10b) nicely conveys this stress argument as Na^+ occupies the sites with lower cationic repulsions (Na2 sites in yellow). It should be noted that the same transitions from O3 to O1' was observed by Yamada and coworkers after removing approximately one Na^+ from Na_2RuO_3.[9] However, further Na^+ deintercalation from Na_2RuO_3 led to complex structural changes, due to the possible Ru migrations which are likely to happen in order to stabilize the highly oxidized structure. In the case of Ir, further removal of 0.5 Na^+ does not result in cationic migration but instead to a complete reorganization of Ir_2O_6 layers to form the O1 structure.

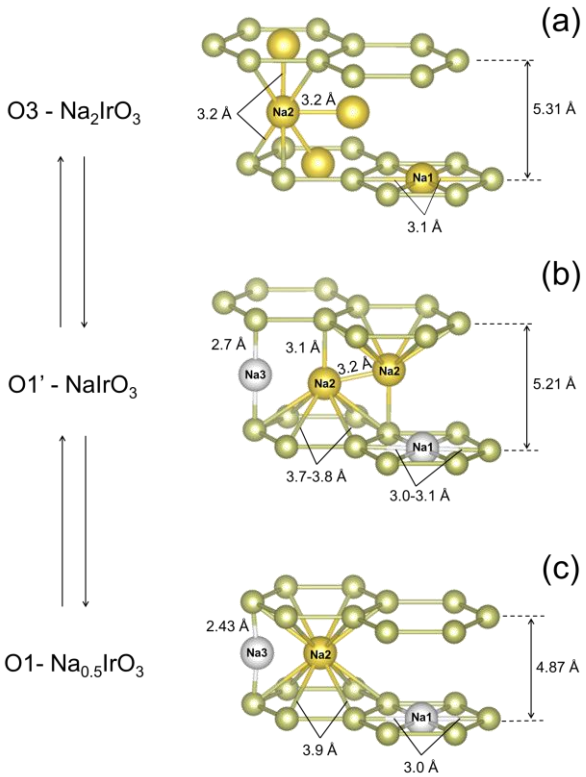

Figure 10

Figure 10c shows that the alignment of honeycombs in the O1 structure creates a site for the remaining 0.5 Na^+ with minimum cationic repulsion (Na2 site) while any extra Na^+ left in the structure will be subject to strong repulsions (Na1 and Na3 sites). The structural stability of this site is most likely at the origin of our inability to electrochemically remove more than 1.5 Na^+ from Na_2IrO_3 as it will hinder the ionic conduction in the two-dimensional planes. Alternative diffusion paths for Na^+ exist and involve either i) its passage through octahedral sites sharing faces with two strongly repulsive Ir ions or ii) its 1D diffusion perpendicular to the layers, through the empty sites in the honeycombs; both of which are quite unlikely. Thus, the structural transition to O1 for Na-rich layered oxides is viewed as the origin of the practical capacity limitation of the material, and the same reasoning can be applied to Li-rich materials undergoing the same structural transition.

It is now important to address the issue of capacity decay in Na_2IrO_3/Na cells. This decay was mitigated by the use of FEC in Na half-cells and by replacing the Na anode by hard carbon in a full Na-ion cell configuration. The best performances (150 cycles with less than 9 % lost) were obtained by replacing $NaClO_4$ with $NaPF_6$ in EC:DMC. This result simply validates the possibility to use Na-rich layered oxides with anionic redox activity as cathode materials for Na-ion batteries. The precise degradation mechanism of the material in Na-half cells remains unclear. FEC is known to form an elastomeric layer at the surface of Na metal, hence minimizing electrolyte decomposition at the Na electrode. Therefore, in absence of FEC, the degradation products coming from the electrolyte decomposition could migrate to the positive electrode and poison Na_2IrO_3.

Last but not least, let us now interrogate further the underlying redox mechanisms pertaining to the Na_2IrO_3 phase, bearing in mind that the high resolution ABF-STEM data

together with neutron diffraction have revealed a distortion of the IrO_6 octahedra leading to the formation of (O-O) dimers. Moreover, XPS has shown that the anionic and cationic redox processes occur simultaneously on the low voltage plateau at 2.7 V vs. Na^+/Na. This contrasts with Li_2RuO_3 for which the two redox processes are well parted with the cationic and anionic redox processes appearing on low and high voltage plateaus, respectively.[4] From this point of view, Na_2IrO_3, by cumulating anionic and cationic redox processes, behaves like Li_2IrO_3.[10] To rationalize such finding, the electronic structure of the pristine Na_2IrO_3 phase was calculated by DFT and the obtained Density of States (DOS) is shown in Figure 11a. It indicates that the bands lying just below the Fermi level involved in the oxidation processes display both a cationic and an anionic contribution, with a slightly greater cationic contribution. As shown by the electron density differences presented in Figure 11b, the removal of two successive Na from the Na_2IrO_3 structure clearly promotes a mixed cationic-anionic redox activity. Interestingly, to the best of our knowledge, Na_2IrO_3 and Li_2IrO_3 are the only materials that show anionic redox activity at the early stage of the Na(Li) removal process. Coincidentally or not, these two compounds are composed of slightly distorted IrO_6 octahedra in their pristine states (see inset of Figure 6a). This distortion may be an indication that, even in the pristine material, we are already in a state where oxygen is not formally 2- due to the extent of covalency. Could such an observation bear some meaning regarding the possibility of using the distortion of the MO_6 octahedra as an indicator of an early activation of the anionic redox activity in these compounds remains an open question. Further examples must be found to validate such a tentative correlation. Note, however, that our calculations support this view since the COOPs analysis of Na_2IrO_3 (see Figure 11a) shows peaks corresponding to the formation of O-O dimers (at 2.6 Å distance) which are slightly oxidized in $(O_2)^{n-}$ species. Such species should be detected by XPS and this is not the case, an issue that remains to be solved. Regardless, at x = 0.5, our calculations confirm the contraction of the O-O

bonds (down to 2.38 Å, in fair agreement with the value obtained from neutron diffraction) in response to the removal of electrons from antibonding Ir-O and antibonding O-O electronic states. Moreover, the projected O-O bond distances along the c-axis are in very good agreement with those measured from high resolution ABF-STEM images (Figure S11).

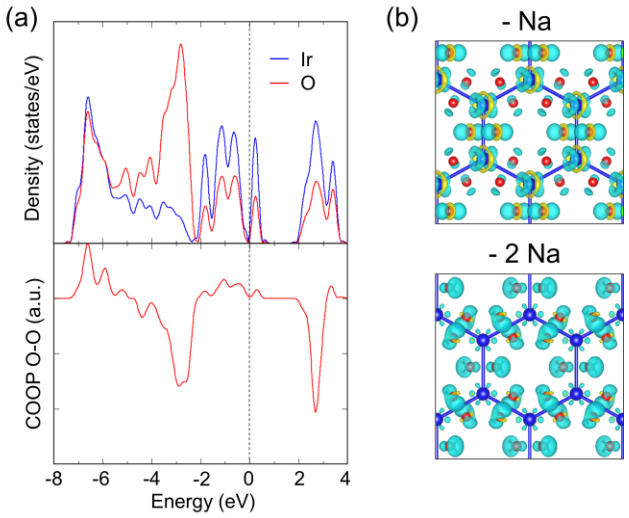

Figure 11

In summary, we demonstrated Na_2IrO_3 to be a model compound for studying the electrochemical performances of Na-rich layered oxides as it eliminates the structural complexity associated to cationic migration and O_2 release encountered for the Li-rich phases. Due to the strong overlap of Ir and O orbitals, the integrity of transition metal layers is preserved upon cycling. This situation leads to a very good reversibility of the anionic redox process, which confirms the use of Na-rich layered oxides as a valid strategy to increase the potential and capacity of Na-ion cathode materials. Therefore, several limits of Na-rich layered oxides were identified. The first one deals with the reorganization of the layers via gliding motions to form the O1 structure that limits, through a stabilization of the Na^+ sites, the deintercalation to ~1.5 Na^+.

This intrinsic structural limitation, which can be extended from Na-rich to Li-rich layered oxides, stands as a warning for the design of high capacity cathode materials. The right compromise, between enhancing the structural rigidity via increasing the M-O bond and weakening the M-O bond to favor structural elasticity as for Ru-based compounds, has to be found. The second limitation is related to the high reactivity of Na-based layered oxides with electrolyte decomposition products, once again highlighting that a proper choice of electrolyte is critical to the performances of a given material. Overall, this work further confirms that the anionic redox activity, recently identified in Li-rich phases, can also be used to design high capacity Na-based electrode materials. This could strongly affect the development of Na-ion batteries provided that we succeed in preparing Na-rich phases based on more abundant metals such as Mn and Fe.

Associated content

Supporting Information. CIF files, Crystallographic data, Rietveld refinements, additional TEM data and DFT results. This material is available free of charge via the Internet at http://pubs.acs.org.

Author information

Corresponding author: jean-marie.tarascon@college-de-france.fr

Notes

The authors declare no competing financial interest.

Acknowledgement

The authors thank Montse Casas-Cabanas and Marine Reynaud for discussions about the FAULTS program, Sandra Van Aert for her great help in guiding us towards the use of the statistical parameter estimation method for establishing the O-O histogram, and Thomas Hansen and Vladimir Pomjakushin for their precious help in neutron diffraction experiments. This work is based on experiments performed at the Swiss spallation neutron source SINQ, Paul Scherrer Institute, Villigen, Switzerland, and at Institut Laue Langevin, Grenoble, France. Use of the 11-BM mail service of the APS at Argonne National Laboratory was supported by the U.S. department of Energy under contract No. DE-AC02-06CH11357 and is greatly acknowledged.

References

(1) Yabuuchi, N.; Kajiyama, M.; Iwatate, J.; Nishikawa, H.; Hitomi, S.; Okuyama, R.; Usui, R.; Yamada, Y.; Komaba, S. P2-Type $Na_x[Fe_{1/2}Mn_{1/2}]O_2$ Made from Earth-Abundant Elements for Rechargeable Na Batteries. *Nat. Mater.* **2012**, *11*, 512–517.

(2) Koga, H.; Croguennec, L.; Ménétrier, M.; Douhil, K.; Belin, S.; Bourgeois, L.; Suard, E.; Weill, F.; Delmas, C. Reversible Oxygen Participation to the Redox Processes Revealed for $Li_{1.20}Mn_{0.54}Co_{0.13}Ni_{0.13}O_2$. *J. Electrochem. Soc.* **2013**, *160*, A786–A792.

(3) Sathiya, M.; Rousse, G.; Ramesha, K.; Laisa, C. P.; Vezin, H.; Sougrati, M. T.; Doublet, M.-L.; Foix, D.; Gonbeau, D.; Walker, W.; Prakash, A. S.; Ben Hassine, M.; Dupont, L.; Tarascon, J.-M. Reversible Anionic Redox Chemistry in High-Capacity Layered-Oxide Electrodes. *Nat. Mater.* **2013**, *12*, 827–835.

(4) Sathiya, M.; Abakumov, A. M.; Foix, D.; Rousse, G.; Ramesha, K.; Saubanère, M.; Doublet, M. L.; Vezin, H.; Laisa, C. P.; Prakash, A. S.; Gonbeau, D.; VanTendeloo, G.; Tarascon, J.-M. Origin of Voltage Decay in High-Capacity Layered Oxide Electrodes. *Nat. Mater.* **2015**, *14*, 230–238.

(5) Foix, D.; Sathiya, M.; McCalla, E.; Tarascon, J.-M.; Gonbeau, D. X-Ray Photoemission Spectroscopy Study of Cationic and Anionic Redox Processes in High-Capacity Li-Ion Battery Layered-Oxide Electrodes. *J. Phys. Chem. C* **2016**, *120*, 862–874.

(6) Yabuuchi, N.; Takeuchi, M.; Nakayama, M.; Shiiba, H.; Ogawa, M.; Nakayama, K.; Ohta, T.; Endo, D.; Ozaki, T.; Inamasu, T.; Sato, K.; Komaba, S. High-Capacity Electrode Materials for Rechargeable Lithium Batteries: Li_3NbO_4-Based System with Cation-Disordered Rocksalt Structure. *Proc. Natl. Acad. Sci.* **2015**, *112*, 7650–7655.

(7) Freire, M.; Kosova, N. V.; Jordy, C.; Chateigner, D.; Lebedev, O. I.; Maignan, A.; Pralong, V. A New Active Li-Mn-O Compound for High Energy Density Li-Ion Batteries. *Nat. Mater.* **2016**, *15*, 173–177.

(8) Rozier, P.; Sathiya, M.; Paulraj, A.-R.; Foix, D.; Desaunay, T.; Taberna, P.-L.; Simon, P.; Tarascon, J.-M. Anionic Redox Chemistry in Na-Rich $Na_2Ru_{1-y}Sn_yO_3$ Positive Electrode Material for Na-Ion Batteries. *Electrochem. Commun.* **2015**, *53*, 29–32.

(9) Mortemard de Boisse, B.; Liu, G.; Ma, J.; Nishimura, S.; Chung, S.-C.; Kiuchi, H.; Harada, Y.; Kikkawa, J.; Kobayashi, Y.; Okubo, M.; Yamada, A. Intermediate Honeycomb Ordering to Trigger Oxygen Redox Chemistry in Layered Battery Electrode. *Nat. Commun.* **2016**, *7*, 11397.
(10) McCalla, E.; Abakumov, A. M.; Saubanère, M.; Foix, D.; Berg, E. J.; Rousse, G.; Doublet, M.-L.; Gonbeau, D.; Novák, P.; Tendeloo, G. V.; Dominko, R.; Tarascon, J.-M. Visualization of O-O Peroxo-like Dimers in High-Capacity Layered Oxides for Li-Ion Batteries. *Science* **2015**, *350*, 1516–1521.
(11) Mikhailova, D.; Karakulina, O. M.; Batuk, D.; Hadermann, J.; Abakumov, A. M.; Herklotz, M.; Tsirlin, A. A.; Oswald, S.; Giebeler, L.; Schmidt, M.; Eckert, J.; Knapp, M.; Ehrenberg, H. Layered-to-Tunnel Structure Transformation and Oxygen Redox Chemistry in $LiRhO_2$ upon Li Extraction and Insertion. *Inorg. Chem.* **2016**, *55*, 7079–7089.
(12) Krizan, J. W.; Roudebush, J. H.; Fox, G. M.; Cava, R. J. The Chemical Instability of Na_2IrO_3 in Air. *Mater. Res. Bull.* **2014**, *52*, 162–166.
(13) Rodríguez-Carvajal, J. Recent Advances in Magnetic Structure Determination by Neutron Powder Diffraction. *Phys. B Condens. Matter* **1993**, *192*, 55–69.
(14) Casas-Cabanas, M.; Rodríguez-Carvajal, J.; Palacín, M. R. FAULTS, a New Program for Refinement of Powder Diffraction Patterns from Layered Structures. *Z. Für Krist. Suppl* **2006**, *23*, 243–248.
(15) Shirley, D. A. High-Resolution X-Ray Photoemission Spectrum of the Valence Bands of Gold. *Phys. Rev. B* **1972**, *5*, 4709–4714.
(16) Scofield, J. H. Hartree-Slater Subshell Photoionization Cross-Sections at 1254 and 1487 eV. *J. Electron Spectrosc. Relat. Phenom.* **1976**, *8*, 129–137.
(17) Kresse, G.; Furthmüller, J. Efficiency of Ab-Initio Total Energy Calculations for Metals and Semiconductors Using a Plane-Wave Basis Set. *Comput. Mater. Sci.* **1996**, *6*, 15–50.
(18) Kresse, G.; Hafner, J. Ab Initio Molecular Dynamics for Liquid Metals. *Phys. Rev. B* **1993**, *47*, 558–561.
(19) Perdew, J. P.; Burke, K.; Ernzerhof, M. Generalized Gradient Approximation Made Simple. *Phys. Rev. Lett.* **1996**, *77*, 3865–3868.
(20) Dudarev, S. L.; Botton, G. A.; Savrasov, S. Y.; Humphreys, C. J.; Sutton, A. P. Electron-Energy-Loss Spectra and the Structural Stability of Nickel Oxide: An LSDA+U Study. *Phys. Rev. B* **1998**, *57*, 1505–1509.
(21) Grimme, S.; Ehrlich, S.; Goerigk, L. Effect of the Damping Function in Dispersion Corrected Density Functional Theory. *J. Comput. Chem.* **2011**, *32*, 1456–1465.
(22) Dronskowski, R.; Bloechl, P. E. Crystal Orbital Hamilton Populations (COHP): Energy-Resolved Visualization of Chemical Bonding in Solids Based on Density-Functional Calculations. *J. Phys. Chem.* **1993**, *97*, 8617–8624.
(23) Deringer, V. L.; Tchougreeff, A. L.; Dronskowski, R. Crystal Orbital Hamilton Population (COHP) Analysis As Projected from Plane-Wave Basis Sets. *J. Phys. Chem. A* **2011**, *115*, 5461–5466.
(24) Maintz, S.; Deringer, V. L.; Tchougreeff, A. L.; Dronskowski, R. Analytic Projection From Plane-Wave and PAW Wavefunctions and Application to Chemical-Bonding Analysis in Solids. *J. Comput. Chem.* **2013**, *34*, 2557–2567.
(25) Delmas, C.; Fouassier, C.; Hagenmuller, P. Structural Classification and Properties of the Layered Oxides. *Phys. BC* **1980**, *99*, 81–85.

(26) Komaba, S.; Ishikawa, T.; Yabuuchi, N.; Murata, W.; Ito, A.; Ohsawa, Y. Fluorinated Ethylene Carbonate as Electrolyte Additive for Rechargeable Na Batteries. *ACS Appl. Mater. Interfaces* **2011**, *3*, 4165–4168.
(27) Lu, H.; Wu, L.; Xiao, L.; Ai, X.; Yang, H.; Cao, Y. Investigation of the Effect of Fluoroethylene Carbonate Additive on Electrochemical Performance of Sb-Based Anode for Sodium-Ion Batteries. *Electrochimica Acta* **2016**, *190*, 402–408.
(28) Wallace, D. C.; McQueen, T. M. New Honeycomb Iridium(V) Oxides: $NaIrO_3$ and Sr3CaIr2O9. *Dalton Trans.* **2015**, *44*, 20344–20351.
(29) Van Aert, S.; Verbeeck, J.; Erni, R.; Bals, S.; Luysberg, M.; Dyck, D. V.; Tendeloo, G. V. Quantitative Atomic Resolution Mapping Using High-Angle Annular Dark Field Scanning Transmission Electron Microscopy. *Ultramicroscopy* **2009**, *109*, 1236–1244.

List of figures

Figure 1. First and second galvanostatic cycles of Na_2IrO_3 vs Na (a), SXRD patterns (b) and high resolution HAADF-STEM images (c-e) of samples at different states of charge. Different stackings of the transition metal layers are found and represented here. For clarity, only the Ir honeycombs are represented in the sketch, and the crystallographic directions corresponding to the TEM observations are indicated. The red lines on the HAADF-STEM images highlight the perfect cubic close-packed ABCABC (c) and hexagonal close-packed ABAB (d, e) stacking of oxygen.

Figure 2. Online Electrochemical Mass Spectrometry data for the first and second cycles, with the voltage curve (a) and the evolution rate of CO_2 and O_2 indicated in black and red respectively (b). The cycling started from the material precharged at 3 V to limit degradation in air while preparing the electrode. A small amount of O_2 is detected at the very end of charge (between dashed lines).

Figure 3. In situ XRD study of Na_2IrO_3 (cycled at C/40 between 1.5 V and 4 V). The pristine O3, O1' and O1 phases are highlighted in blue, pink and red, respectively.

Figure 4. Rietveld refinement of synchrotron X-ray diffraction pattern for the fully charged $Na_{0.5}IrO_3$ (4V). The inset highlights the unusual shape of the first peak, which prevents a good refinement of the data.

Figure 5. Modification of the oxidation states of Ir and O during the first charge. XPS analysis of Ir 4f (a) and O 1s (b) peaks show that both Ir and oxygen are oxidized on the first plateau, and oxygen only on the second plateau. The proportion of $(O_2)^{n-}$ species depending on state of charge is shown in (c).

Figure 6. Refinement of neutron diffraction patterns for the pristine (a) and O1 (b) structures. The insets show the different O-O distances around Ir atoms obtained from neutron diffraction. Complementary [001] HAADF-STEM (c) and ABF-STEM (d) images of the fully charged O1 structure. Magnified fragment of the ABF-STEM image with marked projections of the IrO_6 octahedra (e) and intensity profiles highlighting short and long projected O-O distances (f).

Figure 7. Galvanostatic cycling of Na_2IrO_3 in Na half-cells (C/5 rate - 1 Na^+ in 5h) between 1.5 V and 4 V (a), on the lower or higher plateau (b) vs Na^+/Na, using 1M $NaClO_4$ in EC:DMC with 1 % FEC as an electrolyte. First and 50^{th} cycles are highlighted in blue and red respectively. Capacity retention upon cycling for different cutoff voltages (c).

Figure 8. Synchrotron X-ray diffraction patterns for Na_2IrO_3 discharged after 50 cycles (a). This fit was obtained with a 3 phases model where phase 1 (O3-Na_2IrO_3, blue ticks) and phase 2 (Ir impurity, black ticks) were refined using the Rietveld method, and phase 3 (O1*-Na_xIrO_3, red ticks) was fitted using pattern-matching. Comparison of the experimental pattern to the three isolated components and to the experimental pattern of O1-$Na_{0.5}IrO_3$ (b). TEM data for the discharged sample after 50 cycles demonstrating stabilization of the O1 structure even in the discharged state (c-d).

Figure 9. Galvanostatic cycling of Na_2IrO_3 in a full cell configuration (a) with hard carbon as an anode (C/5, 0 V to 4 V) and using $NaPF_6$ in EC:DMC as an electrolyte. First and 150^{th} cycles are highlighted in blue and red, respectively. Capacity retention and efficiency upon cycling (c).

Figure 10. Possible Na positions for the pristine (a), O1' (b) and O1 (c) structures. Yellow atoms are the occupied positions and white balls represent sites left vacant with strong electrostatic repulsion from neighboring cations. Complete deintercalation of Na^+ in Na3 positions for the O1 structure cannot be achieved due to the very high stability of the site occupied by the last 0.5 Na.

Figure 11. Projected density of states and O-O crystal orbital overlap population (COOP) of Na_2IrO_3 (a). The presence of unoccupied states with a large negative O-O COOP (anti-bonding O-O states) suggests the presence of O-O bonds already in the pristine material. Electron density difference computed by removing 1 (top) and 2 (bottom) sodium from Na_2IrO_3 (b). Ir and O are represented by blue and red spheres, respectively. Light blue volumes correspond to electron density depletion (holes) and yellow regions correspond to electron density accumulation (electrons) due to orbital polarization. Holes are localized on both Ir and O atom after removing the first Na, and mostly on O atoms after all the Na is removed, showing that a mixed cationic and anionic redox is expected for this material.

Synopsis TOC